Investigating the relationship between Langmuir turbulence and ocean mixed layer entrainment in large-eddy simulations (LES)

Undergraduate Senior Thesis

Hannah Kolus

Thesis Committee: Baylor Fox-Kemper and Robert Pelcovits

Brown University Physics Department, 30 April 2015

Abstract

Large eddy simulations, forced with realistic wind stresses at several wave ages, were used to investigate the scaling of peak buoyancy flux with mixed layer depth, for several definitions of mixed layer depth. The mixed layer depth defined by the minimum buoyancy flux corresponded to a slightly nonlinear scaling ($r^2 = 0.929$), with a steeper slope than that found by Grant and Belcher (2009). In the low wind limit, however, the data followed this slope fairly well, suggesting that different scaling laws are required for different wind strengths, since the rate of production of potential energy increases relative to rate of turbulent kinetic energy production at higher wind speeds. Using the base of the buoyancy flux as the mixed layer depth yielded a tight linear and, thus, predictable scaling relationship ($r^2 = 0.980$). This definition may prove more useful for scaling purposes in models that do not resolve these small-scale turbulent features.

Introduction

Motivation

At the ocean's surface, wind, surface cooling, breaking waves, and other turbulent processes induce mixing and convective overturning (Haney, 2015). This mixing takes place in a thin layer of relatively uniform density, temperature, and salinity called the mixed layer. Typical mixed layer depths range globally from tens to hundreds of meters and exhibit both diurnal and seasonal cycles (Garwood, 1974; Cronin and Sprintall, 2000). Since the mixed layer is the interface between ocean and atmosphere, as well as the surface ocean and deep ocean, it controls the exchange of momentum, moisture, and gasses like CO_2 at these boundaries. For example, because of the equilibrium required between the temperatures of the sea surface and the

air sitting above it, the mixed layer regulates the latent, sensible, and radiative heat fluxes between the ocean and the atmosphere (Haney, 2015).

Additionally, the ocean mixed layer influences biological productivity through nutrient and light availability, because the advection of water parcels governs the movement of organisms such as phytoplankton. A deeper mixed layer may expose organisms to additional nutrient sources and increase productivity, but it may also pull organisms beneath the euphotic zone, where light cannot penetrate, thus preventing photosynthesis and decreasing productivity (Sarmiento and Gruber, 2013). The biological impact of the mixed layer also factors into climate change, since photosynthetic organisms consume carbon while living, then export this carbon to the deep ocean by sinking when they die. This can be considered a long-term sink of carbon, since the time scales governing the thermohaline circulation that returns water from the deep ocean back to the surface extend up to 1000 years (Sarmiento and Gruber, 2013).

Since the mixed layer plays such a significant role within the Earth system, it is desirable to understand the physical processes that control its properties. Currently, grasping the dynamics that influence the mixed layer is of particular interest, since rising global temperatures and climate change have emerged as significant threats to the future habitability of the planet. One mechanism that strongly affects mixed layer properties is turbulent mixing resulting from unstable Langmuir circulation. Langmuir circulation, illustrated in figure 1, is characterized by an array of vortices, termed Langmuir 'cells', alternating in sign and oriented with their horizontal axes downwind (Thorpe, 2004). While this kind of turbulent mixing occurs on small scales compared to typical ocean scales, it influences mixed layer dynamics enough to have a potentially significant impact on global scale dynamics (Belcher et al., 2012; D'Asaro et al., 2014; Li et al., 2015).

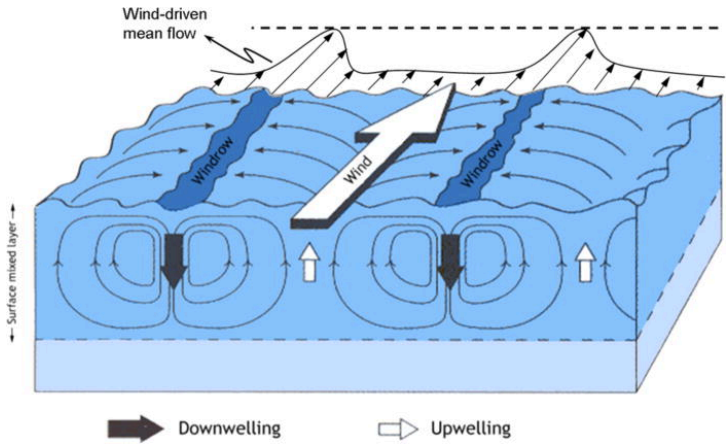

Figure 1. Illustration of the mean flow in idealized Langmuir circulation. The wind creates parallel divergent zones of upwelling. In between these zones, the water converges and downwells. The wind-driven mean flow is directed downwind. (Tejada-Martinez et al., 2011).

At the moment, Langmuir turbulence is absent from general circulation models (GCMs). An inclusion of a turbulence parameterization may improve GCMs' agreement with ocean observations and move modelers a step closer towards accurately predicting future climate scenarios. Several recent studies have used large eddy simulations (LES) to develop scaling laws between the parameters that force turbulence (e.g. wind) and proxies for the strength of the turbulent response (e.g. vertical kinetic energy) (Grant and Belcher, 2009; Harcourt and D'Asaro, 2008; Van Roekel et al., 2012). For this study, LES simulations were performed using parameters derived from Harcourt and D'Asaro (2008), monochromatic waves, and the Coriolis parameter set to zero. One main goal was to reproduce a previous scaling law determined by Grant and Belcher (2009) relating mixed layer depth with a scaling velocity and the minimum buoyancy flux. However, exactly how the mixed layer depth should be determined is unclear. Cronin and Sprintall (2000) define it as the depth at which the temperature is 0.5°C cooler than the surface temperature; this definition is more helpful from an observational standpoint, since it is easy to measure. Grant and Belcher (2009) define it as the depth corresponding to the

minimum of the vertical buoyancy flux profile – a description related more to the turbulent dynamics of the surface ocean. However, this definition ignores the potential variations in the overall shape of the buoyancy flux profile, which could influence whether entrainment of deeper water across mixed layer base is quantified accurately. Therefore, this study also introduces a new definition of mixed layer depth, defined as the depth corresponding to the base of the buoyancy flux profile. From a conceptual standpoint, this new definition focuses on identifying the maximum possible depth to which turbulence can extend, while also embodying Grant and Belcher's concept of the depth at which turbulent transport is most important. Scaling was applied using this new definition and the accuracy compared with the previous scalings.

Theory

I. Stokes drift

The Langmuir cells illustrated in figure 1 come about through the interaction of vorticity and Stokes drift of surface waves (Van Roekel et al., 2012). The Stokes drift velocity can be derived starting from Lagrangian and Eulerian velocities. For a particle that started at position $\boldsymbol{x}_0$, the Lagrangian ($\boldsymbol{u}_L$) and Eulerian ($\boldsymbol{u}_E$) velocities are related to each other at time t by the equation (Garrett, 2004):

$$\boldsymbol{u}_L(\boldsymbol{x}_0,t) = u_E\left(\left[\boldsymbol{x}_0 + \int_0^t \boldsymbol{u}_L(\boldsymbol{x}_0,t')dt'\right],t\right) \tag{1}$$

where parentheses denote the position and time at which the velocities are evaluated. The Stokes drift velocity is the difference between the mean Lagrangian flow velocity (of a single water parcel) and Eulerian flow velocity (at a fixed point). Conceptually, it is the average velocity that a specific water parcel experiences as it travels with the overall fluid flow. The Stokes drift

velocity can be derived using the barotropic, inviscid, irrotational, incompressible flow solutions to deep water gravity waves (monochromatic): $u = \frac{\partial \phi}{\partial x}$ and $w = \frac{\partial \phi}{\partial z}$ with potential velocity $\phi = A\frac{\omega}{k}e^{kz}\sin(kx - \omega t)$. Here, A is the wave amplitude, k is the wavenumber, and ω is the wave frequency. These deep-water waves follow the dispersion relation $C_P = \sqrt{\frac{g}{k}}$ (also equation 18 in the *Model Description and Setup* section). Averaging equation (1) in time, expanding for small intervals in space, and assuming that $\boldsymbol{u}_L \approx \boldsymbol{u}_E$ yields the following relation (Garrett, 2004; Haney, 2015):

$$\boldsymbol{u}_S = \left\langle \int_0^t u_E \, dt \cdot \nabla u_E \right\rangle \tag{2}$$

The brackets denote the average, taken over a time longer than the wave period but shorter than the period over which the current changes (Haney, 2015). Evaluating equation (2) using the specific flow solutions given above yields the following equation for Stokes drift at a depth z (note that z is negative below the surface):

$$\boldsymbol{u_s}(\mathrm{z}) = \omega \boldsymbol{k} A^2 e^{2kz} \tag{3}$$

The exponential component of equation (3) can also be written as $exp(z/D_s)$, where D_s is the Stokes e-folding depth.

II. Langmuir Turbulence

The turbulent Langmuir number, introduced by McWilliams et al. (1997) is an important nondimensional parameter for characterizing Langmuir turbulence. It is defined as

$$La_t = \sqrt{\frac{u^*}{U_S}} \tag{4}$$

where U_s denotes the surface Stokes drift, $\boldsymbol{u_S}(0)$, and u^*, the surface friction velocity, is given by

$$u^* = \sqrt{\frac{\tau}{\rho_0}} \tag{5}$$

Here, τ represents the wind stress at the surface of the ocean, and ρ_0 is the mean density of the water. Therefore, the Langmuir turbulent number evaluates the relative strength of wind versus waves: small $La_t << 1$ indicates that wave effects dominate wind effects, inducing high turbulence (Haney, 2015).

III. Reynolds decomposition

The velocity and temperature/buoyancy fields can be separated into large-scale and small-scale components (Reynolds, 1895):

$$\begin{aligned} u &= \bar{U} + u' \\ v &= \bar{V} + v' \\ w &= \bar{W} + w' \\ T &= \bar{T} + T' \end{aligned} \tag{6}$$

where (u, v, w) corresponds to flow in the (x, y, z) directions and z is negative below the ocean surface. In these equations, the large-scale component, denoted by an overbar, is the mean quantity, while the primed term signifies the fluctuations about the mean. In this study, horizontal averages over the domain and averages over a sliding window of time will define the meaning of variables with overbars. These components satisfy the following spatial averaging conditions:

$$\frac{1}{N_{i,j}} \sum_{i,j} u(z) = \bar{U} \tag{7}$$

$$\sum_{i,j} u'(z) = 0 \tag{8}$$

where i and j are the horizontal (x, y) indices over which the averaging takes place and $N_{i,j}$ denotes the total number of grid cells in the horizontal plane at depth z. Any solitary fluctuating

component averages to zero, but average of the product of two fluctuating components is nonzero. Thus, finding the product of two fluctuating components requires subtracting the mean from the total as follows:

$$\frac{1}{N_{i,j}}\sum_{i,j}(u-\overline{U})^2 = \overline{u'^2} = \sigma_u^2 \qquad (9)$$

Calculation of the variance of the vertical velocity, $\overline{w'^2}$, is simplified by the fact that the mean vertical flow equals zero, so that $w = w'$. Another quantity of interest for this study, the buoyant production (see the *Turbulent kinetic energy budget* section below), is calculated as

$$\frac{1}{N_{i,j}}\sum_{i,j}\alpha g w(T-\overline{T})^2 = \overline{w'b'} \qquad (10)$$

where α is the fluid's thermal expansion coefficient, g is the acceleration due to gravity, and b is the buoyancy.

IV. Turbulent kinetic energy budget

The turbulent kinetic energy (TKE) is defined as $\frac{1}{2}\left(\overline{u'^2}+\overline{v'^2}+\overline{w'^2}\right)$. For horizontally uniform conditions and assuming that the rate of change of TKE with time is zero, the TKE budget can be written as (Grant and Belcher, 2009):

$$\frac{\partial(TKE)}{\partial t} = -\overline{u'w'}\frac{\partial\overline{U}}{\partial z} - \overline{v'w'}\frac{\partial\overline{V}}{\partial z} - \overline{u'w'}\frac{\partial u_S}{\partial z} + \overline{w'b'} - \frac{\partial}{\partial z}\left(\overline{w'E'} + \frac{1}{\rho}\overline{w'p'}\right) - \epsilon = 0 \qquad (11)$$

where $\overline{U}$ and $\overline{V}$ denote the mean flow in the $\hat{x}$ and $\hat{y}$ directions, and are also taken to be, respectively, parallel and perpendicular to the surface wind stress; overbars denote averages; ρ is the fluid density; E' is synonymous with TKE; and Stokes drift is parallel to the surface wind stress. The first two terms are shear production terms, which transfer kinetic energy from the mean flow to the turbulent flow through the current shear. The third term is the Stokes production term, which functions similarly to the shear production terms but through the Stokes

shear. The fourth term, $\overline{w'b'}$, is the buoyant production (also called the buoyancy flux), which either generates TKE with a corresponding loss of potential energy (negative $\overline{w'b'}$) or generates potential energy and destroys TKE (positive $\overline{w'b'}$) through buoyancy forces. The fifth term expresses the transportation of TKE within the fluid through turbulent fluctuations in vertical velocity and pressure. The final term, ϵ, is the dissipation rate resulting from molecular viscosity.

Grant and Belcher (2009) showed that the Stokes shear dominates the generation of TKE at the surface and sources the TKE for the vertical component of current. They further showed that the vertical component of the transport term, responsible for delivering the Stokes shear-produced TKE from the surface to lower depths, is much greater than the horizontal component when wave effects are included (as opposed to shear turbulence alone; Grant and Belcher, 2009). Noting these TKE budget balances, Grant and Belcher (2009) suggested a velocity and length scale for the TKE resulting from Langmuir turbulence that depends on the Stokes shear term, $\overline{u'w'}\frac{\partial u_S}{\partial z}$. The following is a brief explanation of their derivation of these length and velocity scales.

Grant and Belcher (2009) designated the mixed layer depth, defined as the depth at which the buoyancy flux reaches a minimum, as the relevant length scale, since the transport of TKE from the surface extends all the way through the mixed layer (Grant and Belcher, 2009). At the surface, $\overline{u'w'}$ is determined by the wind stress (τ), so this term can be represented by u^{*2} (from equation 5). Similarly, averaging $\frac{\partial u_S}{\partial z}$, derived from the Stokes e-folding depth (D_S) version of equation (3), over the mixed layer (h) yields:

$$\frac{1}{h}\int_{h}^{0}\frac{\partial u_S}{\partial z}dz = \frac{U_S}{hD_S}D_S e^{z/D_S}\Big|_{h}^{0} \approx \frac{U_S}{h} \tag{12}$$

where the final simplification is made by assuming that the Stokes e-folding depth is much smaller than the mixed layer depth. Combining these two results, Grant and Belcher (2009) suggest that the Stokes shear production term can be represented by $(u^{*2}U_S)/h$, which can be separated into the aforementioned length scale and the velocity

$$w_L^* = (u^{*2}U_S)^{1/3} \tag{13}$$

According to Grant and Belcher (2009), the term $\frac{w_L^{*3}}{h}$ quantifies the rate of generation of TKE. Thus, plotting it against the buoyancy flux should reveal the relationship between the generation of TKE and the generation of potential energy. The buoyancy flux is associated with the entrainment of cold water into the mixed layer and, consequently, has the potential to deepen (and cool) the mixed layer significantly.

Model Description and Setup

The LES model used for this study was first developed at NCAR (Moeng, 1984) and adapted by McWilliams et al. (1997) to include Stokes drift. The model uses spatially filtered CL equations (McWilliams et al., 1997):

$$\frac{\partial \rho}{\partial t} + \boldsymbol{u}_L \cdot \nabla \rho = SGS \tag{14}$$

$$\nabla \cdot \boldsymbol{u} = 0 \tag{15}$$

$$\frac{\partial \boldsymbol{u}}{\partial t} + (\boldsymbol{\omega} + f\hat{\boldsymbol{z}}) \times \boldsymbol{u}_L = -\nabla \pi - \frac{g\rho\hat{\boldsymbol{z}}}{\rho_0} + SGS \tag{16}$$

where the Lagrangian velocity $\boldsymbol{u}_L = \boldsymbol{u} + \boldsymbol{u}_S$, the Eulerian vorticity is $\boldsymbol{\omega} = \nabla \times \boldsymbol{u}$, the Coriolis parameter is f, g is the acceleration due to gravity, ρ_0 is a reference density, SGS stands for subgrid-scale terms representing processes unresolvable within the grid resolution, and π is the effective pressure, given by:

$$\pi = \left(\frac{p}{\rho_0} + \frac{1}{2} \left| \boldsymbol{u}_L \right|^2 \right) \tag{17}$$

where p is the thermodynamic pressure.

Harcourt and D'Asaro (2008) outlined a simulation set ($\sum_1$) for several wave spectrums of different wave age in combination with a series of realistic wind stresses. This simulation set forms the basis for the model parameters used in this study. Values of U_s were taken directly from the simulation set and corresponding values of u^* were calculated by choosing a constant La_t = 0.3 in equation (4). This is the typical value found through ocean observations and corresponds to fully developed waves (Thorpe, 2004; Haney, 2015). To reiterate, the range of u^* used within this study, approximately 0.009 – 0.05 m/s, results from inputting Harcourt and D'Asaro's surface Stokes drift values into equation (4) and fixing La_t at 0.3. The World Meteorological Organization's *Guide to Wave Analysis and Forecasting* uses a reference surface friction velocity of 0.01 m/s for $U_{10} \approx 8$ m/s (Bouws, 1998). This agrees with the lowest wind case of this study's simulations and its corresponding u^*. The Stokes e-folding depth, D_s, was calculated from the non-dimensional parameter $2k_pD_s$ provided by Harcourt and D'Asaro using the relation

$$C_p = \sqrt{g / k_p} \tag{18}$$

where C_p and k_p are, respectively, the phase speed and the wavenumber of the peak wave in the spectrum. This study simulates monochromatic waves rather than a spectrum, so C_p and k_p were

treated as the phase speed and wavenumber of this monochromatic wave (for implications of using a wave spectrum versus monochromatic waves, see Webb and Fox-Kemper, 2011 and 2015). See the Appendix for the complete table of simulation parameters.

All simulations used a 128 x 128 x 126 meter grid with 2-meter resolution. The Coriolis parameter was set to zero for simplification and minimal computation time, since the Coriolis force introduces inertial oscillations, and the averaging time over which turbulence statistics take place must be subsequently large. Thus, the simulations correspond to an arbitrary location along the equator. Temperature was initialized with a simple function that decreases linearly with depth, and no surface heat flux or cooling was applied. The initial horizontal velocity fields were set zero, with contributions coming only from Stokes drift forcing, then randomly perturbed in order to initiate turbulence. For each simulation, wind and waves were aligned.

Since LES was initialized with arbitrary conditions, it was necessary to account for a spin-up period at the beginning of each simulation during which the system evolved into a fully turbulent state. Other types of models, such as terrestrial biosphere models that simulate carbon cycles and vegetation growth, have relatively clear spin-up conditions whereby the system reaches a steady state. However, the very nature of turbulent flow as chaotic dictates that only a quasi-steady state can be achieved. This is particularly problematic when entrainment is involved, since this implies that the boundary layer defining the base of the mixed layer cannot be fixed: new water is being added continuously. The number of time steps required for each run were roughly approximated beforehand to minimize computation time while ensuring that the simulation spent enough time in a fully turbulent state to produce statistically robust averages of the turbulent characteristics. The ratio of mixed layer depth to surface friction velocity $\left(H_{ML}/u_*\right)$ yields an approximate measure for the mixing time required to bring the system from its

initialized state into a turbulent state, since it is reasonable to assume that this ratio is proportional to the eddy turnover time. This means that a simulation of lower wind speed requires more time to become fully turbulent. A test run at the lowest simulation wind speed produced an average mixed layer depth (as defined by temperature) of about 20 meters. Using this as the baseline mixed layer depth, the range of time scales for spin up calculated with the above ratio extended from about 2000 seconds at the lowest wind speed to 400 seconds at the highest. It should be noted that the mixed layer deepens with higher wind speeds, suggesting that this approximation underestimates the higher wind spin up time; however, since the average mixed layer depth does not vary between simulations as drastically as u^*, the time scale associated with the lowest wind simulation represents the upper bound on spin up time.

The model uses time steps of variable duration in order to minimize numerical instability: as flow velocities increase, the time steps shorten. This means simulations of higher wind stress or wave age are allocated shorter time steps. These variable time steps complicate the direct conversion of the above crudely estimated time scale into number of time steps. The lowest wind case, corresponding to the largest time steps, yielded a range of increments from about 3.5 to 6 seconds over the course of a test run. A similar test run for the highest wind setting yielded time steps of 1 to 1.5 seconds, the lower bound for the entire simulation set. The duration of the simulations was set to 5000 time steps, since this allows for the mixing time to repeat several times even when assuming the longest spin up time and the shortest time step. Data files were output every fifty time steps for each run. It should be noted that a more thorough analysis of the impact on data output frequency, specifically for higher frequencies (see figure 3 for a basic analysis of the impact of lower frequency data output), would be required to ensure that the results of the following section generalize.

Results

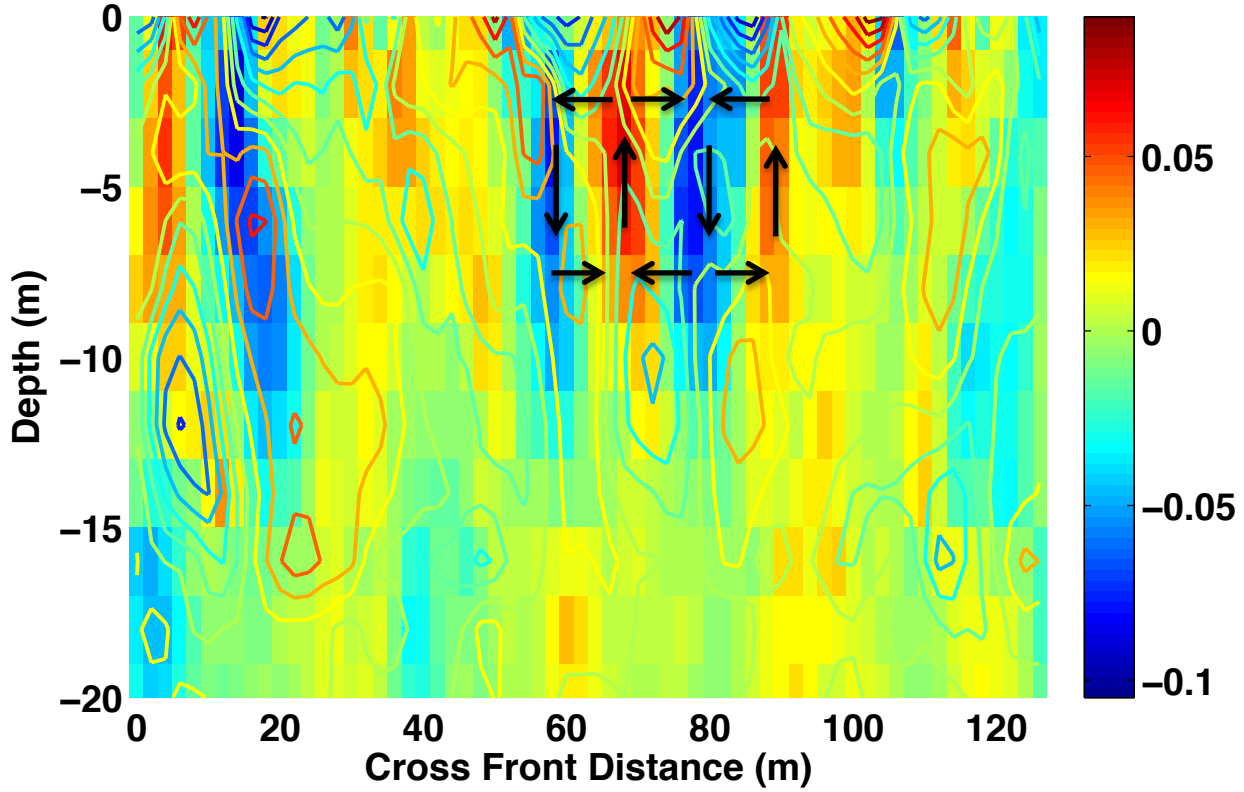

Figure 2. Snapshot of a cross-section of *x* at time step 2050 for an example simulation (medium wind, medium wave age). The background color indicates vertical velocity (*w*), and the superimposed contours denote the current parallel to the y-axis (*v*). Arrows indicate general flow patterns. It should be noted that the color bar applies only to the vertical velocity. Also note that the vertical scale does not extend to the domain boundary. Both velocities have units m/s.

Figure 2 depicts a cross-section of the domain, perpendicular to the *x*-axis, at a time by which several eddy turnovers have taken place, for an example simulation of medium wind and wave age. The background colors correspond to the vertical velocity, and the contours represent the horizontal current flow parallel to the *y*-axis. The characteristics of Langmuir circulation are evident in the upper 10 meters of the domain and especially clear between 60 and 100 meters across the front. Arrows are drawn for clarity, indicating the how the horizontal flow perpendicular to the wind stress and the vertical flow combine to form vortices of alternating sign. However, this pattern is not uniform across the domain, and snapshots at different time steps (not shown) reveal that the vortices deform with time, changing shape, location, and

magnitude. In short, it is clear that figure 1 is, in fact, an ideal case of Langmuir circulation, compared to the Langmuir turbulence exhibited in the LES output. Consequently, it is necessary first to determine when the flow becomes fully turbulent and then to average the flow fields over a large enough interval of time to capture the turbulent statistics that reliably characterize the flow.

The variance of vertical velocity, σ_w^2, also a measure of vertical kinetic energy, can indicate the development of the turbulent quasi-steady state. At the onset of each model run, energy is injected into the domain at the ocean's surface through wind. Through mixing, the energy propagates down, extending to greater and greater depths. This increases the total vertical kinetic energy, integrated over the water column, and influences the shape of the vertical σ_w^2 profile, since the depth corresponding to maximum σ_w^2 also propagates away from the surface. Initially, these changes occur quickly and all in the same direction, moving energy steadily away from the surface. After a certain amount of time, the changes observed in σ_w^2 proceed at a slower rate and oscillate between increasing and decreasing the maximum value of σ_w^2. While the profile of σ_w^2 continues to change, these conditions indicate that the system has reached a quasi-steady state. To assess whether the domain met these conditions in each simulation, σ_w^2 was spatially averaged in the horizontal plane at each depth, producing a vertical profile every fifty time steps (corresponding to each data output file). These vertical profiles were then averaged over several different time spans and compared in order to evaluate of the rate of change of σ_w^2 with time.

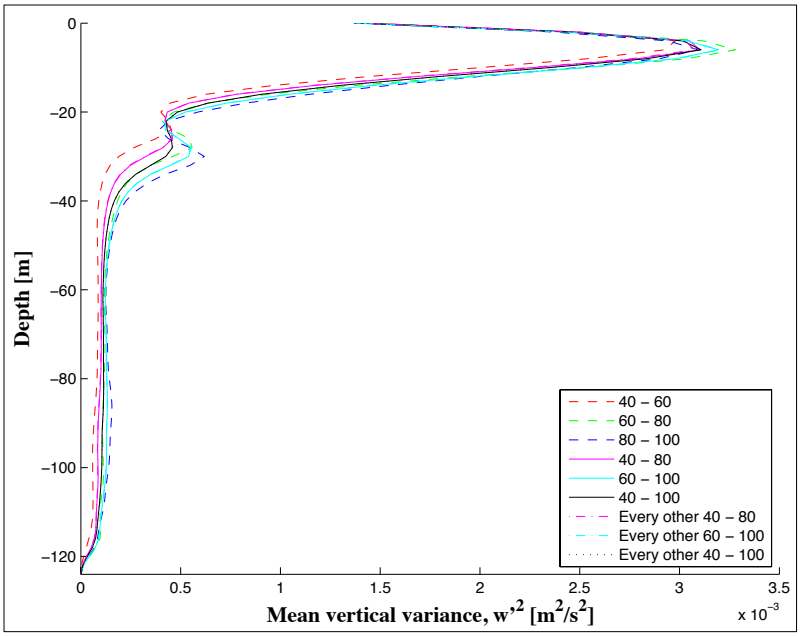

Figure 3. Example plot of the variance of vertical velocity, also a measure of vertical kinetic energy, for U_{10} = 25.8 m/s and C_p/U_{10} = 0.8. The different colors and types of line indicate the output files over which the data averaging took place. For context, the 40th data file falls around the middle of each simulation, and the 100th is the final file. The final three curves were generated by averaging over every other data output file over the given range.

Figure 3 provides an example of how the variance of vertical velocity evolves after spin up, when the system has become a fully developed turbulent flow field. The curves of the plot indicate how the variance changes depending on the intervals over which data averaging took place. Even though the averaging ranges are fairly spread out, the variance curves are generally consistent with each other, with only a small amount of spread at the local maximums. The red, green, and blue dashed curves were generated by averaging over non-overlapping, consecutive time intervals. Thus, when read in order, these three curves give an idea of how the vertical velocity variance changes in time. At the point of maximum variance, around a depth of 10 m, the green curve surpasses the blue slightly, indicating that the variance no longer increases monotonically. Figure 3 also provides some validation for the arbitrary choice to analyze data every 50 time steps. The curves generated by averaging over every other time step virtually

disappear behind the curves of corresponding ranges averaged over each time step. This suggests that the specific choice of data output frequency should not affect the interpretation of results. It should be noted, however, that the influence of data output frequency remains untested for frequencies higher than the output frequency designated for all simulations (e.g. it is unknown whether analyzing data every 25 time steps influences results). For the remainder of the analysis, all vertical profiles were obtained by averaging both spatially in the horizontal plane and temporally over data output files 60 – 100. Error bars for all plots were generated through the calculation, at each depth, of the standard deviation of the spatially-averaged vertical profiles corresponding to each time step. Thus, the error bars reflect variation in time rather than space.

Figure 4 provides examples of mean temperature profiles and $\overline{w'^2}$ profiles for several different simulations corresponding to C_p/U_{10} = 1.2 and a range of wind speeds U_{10} = 8.3, 14.8, 25.8, 32.6 m/s. The mean temperature plots indicate, as expected, that increasing the magnitude of surface winds deepens the ocean mixed layer (as defined by temperature) and decreases the sea surface temperature. The shape of the profiles remains consistently elbow-like, exhibiting a nearly vertical line that extends down from the surface before decreasing sharply in a smooth bend. Towards the bottom of the plot (note that this is not the bottom of the domain) profiles all meet along the linearly decreasing function with which temperature was initialized at the beginning of each simulation. The $\overline{w'^2}$ plots indicate that increasing wind stress increases both the width and amplitude of the vertical velocity's variance and deepens the location of maximum variance. Again, this agrees with expectations, since wind drives mixing, which increases vertical kinetic energy. Below the depth of the peak value, the variance falls fairly quickly to about zero, indicating that mixing largely takes place at the surface and does not extend to the domain's lower boundary.

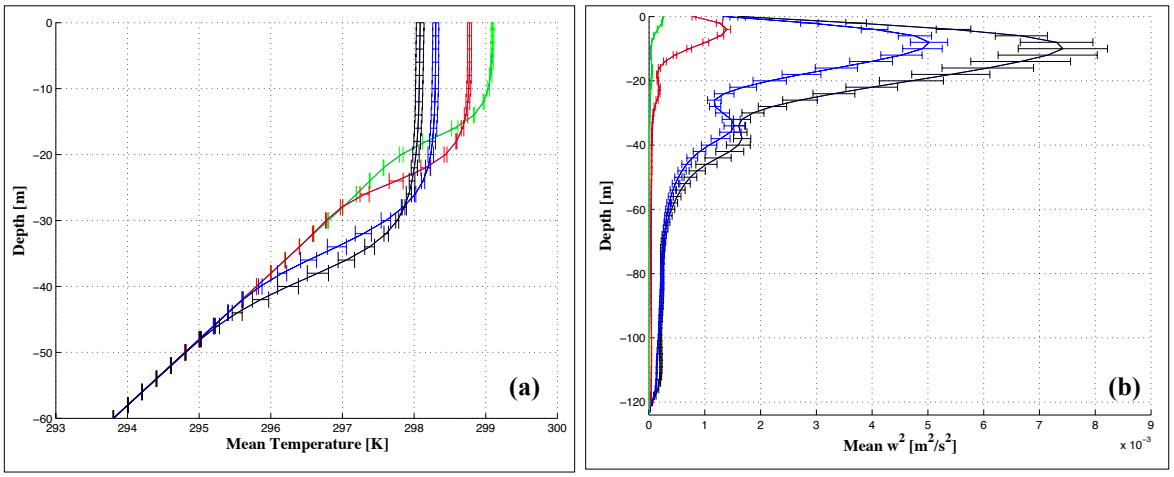

Figure 4. Example plots of mean temperature (a) and $\overline{w'^2}$ (b) for U_{10} = 8.3 m/s (green), 14.8 m/s (red), 25.8 m/s (blue), and 32.6 m/s (black), all with C_p/U_{10} = 1.2. Error bars denote ±1σ. Note that the temperature plot does not extend to the maximum depth.

Figure 5 plots several $\overline{w'b'}$ profiles corresponding to the same simulation cases as figure 3, excluding the lowest wind case. The negative values indicate that the surface mixing transports colder water upward and warmer water downward, increasing potential energy. The buoyancy flux curves follow similar trends to the $\overline{w'^2}$ plots with increasing wind speed: the magnitude and depth of the minimum point increases, stretching both the amplitude and the width of the $\overline{w'b'}$ profiles. The black crosses along the $\overline{w'b'}$ = 0 axis indicate the depth of the mixed layer, calculated as the depth at which the temperature becomes more than 0.5°C lower than the sea surface temperature. Using this definition, it appears that increased wind forcing extends the base of the $\overline{w'b'}$ curve below the depth of the temperature-derived mixed layer. The error bars around the base of the curves are particularly large, suggesting that this region undergoes even greater change over the averaging window than the peak point does. It should be noted that the surface buoyancy flux should return to zero, though this is not the case in the presented curves. The nonzero surface buoyancy flux is a result of the exclusion of unresolved

subgrid terms. Since the subgrid terms are much smaller than the resolved products, they were neglected for the purposes of this study.

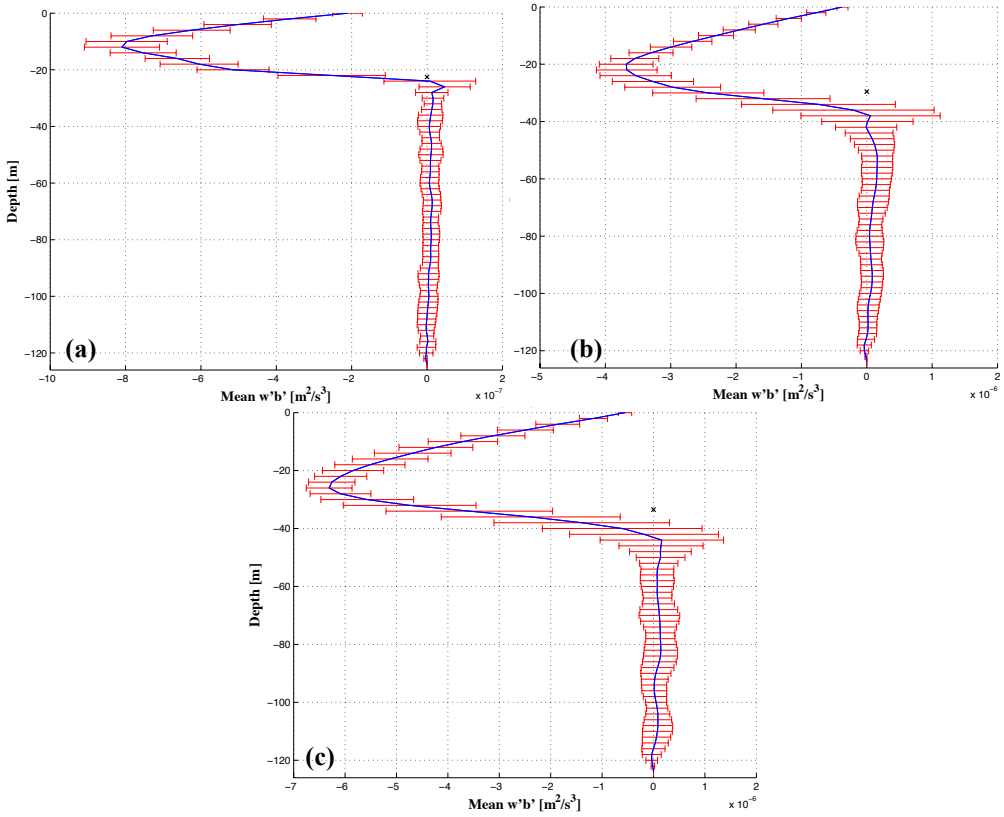

Figure 5. Example plots of mean buoyancy flux, $\overline{w'b'}$ for U_{10} = 14.8 m/s (a), 25.8 m/s (b), and 32.6 m/s (c), all with C_p/U_{10} = 1.2 (the same conditions as in figure 3, excluding the smallest wind case). Error bars denote ±1σ. The 'x' positioned along the $\overline{w'b'}$ = 0 axis indicates the mixed layer depth, calculated from temperature. For each simulation, the buoyancy flux should go to zero at the surface, but is prevented from doing so by unresolved subgrid terms.

From figure 5, it is evident that the buoyancy flux curves are approximately triangle-shaped. Therefore, the area of a $\overline{w'b'}$ curve is well-represented, to a first-order approximation, by two triangles, one that spans the top half of the curve and one that spans the bottom half (see figure 5 for a schematic). The vertices of these triangles overlap at the peak in buoyancy flux and the point at which the depth of the peak intersects the line x = 0. The surface buoyancy flux was assumed to reach zero. Equating the sum of these two triangles with the total area under the

curve (representative of the total rate of change of potential energy) yields an approximation of the buoyancy flux base, since the lower triangle depends on this depth:

$$\frac{\partial}{\partial t} PE = \int_H^0 \overline{w'b'} dz = \frac{1}{2}\left[\left(h * \overline{w'b'}_{min}\right) + (H - h) * \overline{w'b'}_{min}\right] \quad (19)$$

where $\overline{w'b'}_{min}$ is the peak buoyancy flux, h is the depth of this peak, H is the depth of the base, and PE is the potential energy. Simplifying this equation yields the following equation for H:

$$H = \frac{2\frac{\partial}{\partial t}(PE)}{\overline{w'b'}_{min}} \quad (20)$$

The potential energy of each curve was calculated by the midpoint Riemann sum method, and then used to calculate H. Figure 6 depicts a schematic of the triangles that approximate the curve's area. The depths h and H used to define the ideal triangles are indicated. The value of H calculated using equation (20), however, corresponds to the black cross and falls somewhat lower than the ideal bottom triangle's vertex. This indicates that the triangles slightly underestimate the potential energy, which is plainly visible from figure 6.

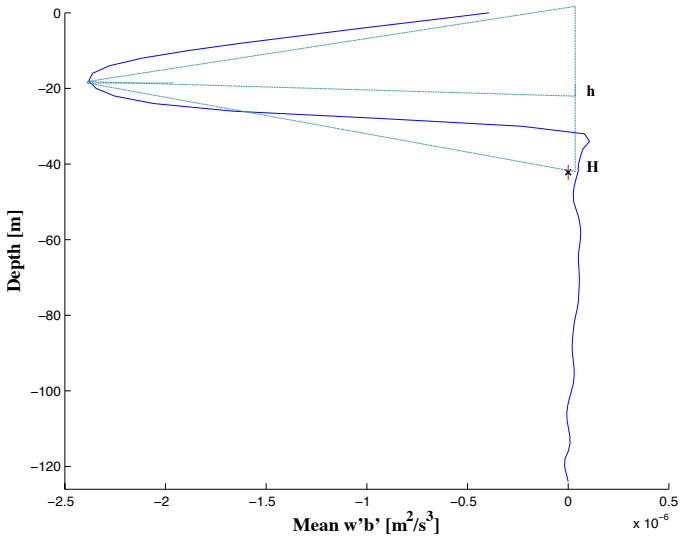

Figure 6. Example plot of the mean buoyancy flux, overlaid with a dotted schematic of the two triangles used to approximate the total potential energy. The labeled depths correspond to the peak in buoyancy flux (h) and the base of the buoyancy flux curve (H). The base of buoyancy production calculated using this methodology, has been indicated by 'x'. The error bars denote ±1σ.

Grant and Belcher (2009) found that $w^*_L = (u^{*2}U_s)^{1/3}$ and the mixed layer depth, defined as the depth of the minimum in the buoyancy flux profile, are the velocity and length scales of Langmuir turbulence. Three variations of this scaling are plotted in figure 7. Figure 7a plots the buoyancy flux scaled by the same definition of mixed layer depth that Grant and Belcher (2009) used. Figure 7b presents a scaling using a temperature-based definition of mixed layer depth, where the temperature is lower than the sea surface temperature by 0.5°C. Figure 7c defines mixed layer depth as the base of the buoyancy flux curve (H). Linear fits have been superimposed on each graph. The mixed layer depth defined using the minimum buoyancy flux yields a slightly non-linear relationship ($r^2 = 0.929$) compared to the temperature and base depth definitions ($r^2 = 0.977$ and 0.980, respectively).

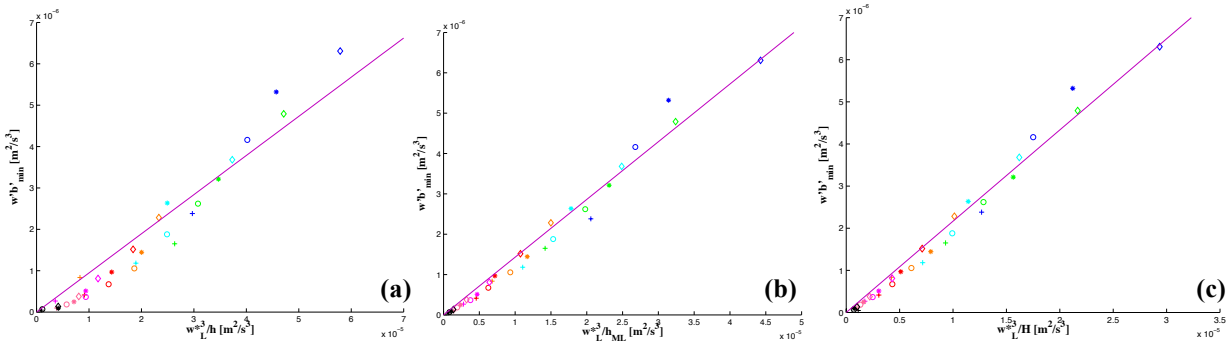

Figure 7. Minimum buoyancy flux scaled by $w^*_L{}^3$ and the mixed layer depth for three different definitions of mixed layer depth: (a) depth corresponding to minimum $\overline{w'b'}$, (b) depth where T < $T_{surface}$ - 0.5°C, (c) depth corresponding to the calculated base of the $\overline{w'b'}$ curve. Each point corresponds to a different simulation. Colors indicate wind speed, and marker shapes indicate wave age. The linear fits superimposed on the plots have slopes (from left to right) 0.095, 0.143, and 0.217 and r^2 values of 0.929, 0.977, and 0.980.

The slopes of the lines are also somewhat different from each other. The mixed layer defined by buoyancy flux base yields the largest slope of 0.217, while the temperature-based mixed layer produces a slope of 0.143. Using the minimum buoyancy mixed layer definition yields the smallest slope of 0.095, but this is still approximately twice as large as the 0.045 slope Grant and Belcher (2009) found. Since this study uses much larger wind stresses than Grant and

Belcher (2009), figure 8 zooms in closer to their range to allow for a better comparison. The red box in the lower left corner indicates the limits of their equivalent plot, and the dotted line indicates the 0.045 slope they found. Only one data point from this study falls within the red box. However, the data points an order of magnitude away from the box still seem to follow the scaling found by Grant and Belcher (2009) rather than the steeper slope found over the complete range of data points.

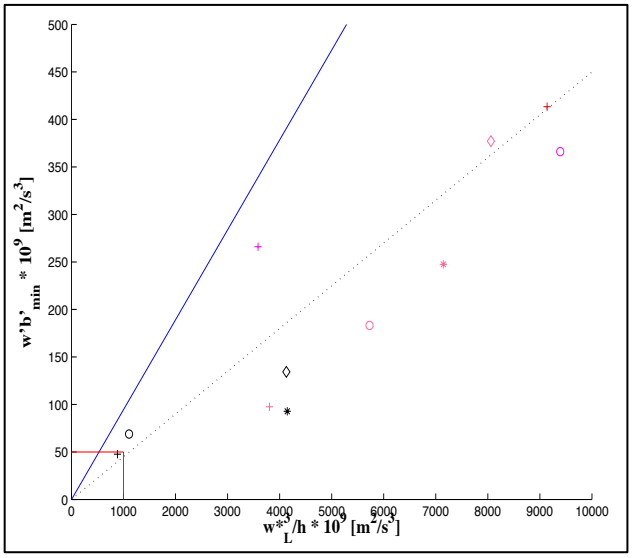

Figure 8. A comparison of the scalings derived from the mixed layer depth defined by the minimum buoyancy flux. The blue line indicates the scaling result determined by this study (slope = 0.095). The dotted line indicates the scaling Grant and Belcher (2009) found (slope = 0.045), and the red box indicates the region in which their simulations were concentrated. Note that the axes have been multiplied by 10^9.

Grant and Belcher found that the ratio of $\overline{w'b'}_{min}$ to $\frac{w_L^{*3}}{h}$ remains constant over a range of turbulent Langmuir numbers. To test this, additional simulations were created for $0.1 \leq La_t \leq 0.9$ and applied to two wind cases, U_{10} = 14.8 and 28.2 m/s, at the highest and lowest wave ages (see Appendix). These wind speeds span the majority of the range tested in the previous simulations. Due to time considerations, data output from these simulations was treated with the same averaging processes as outlined earlier. It is possible that some of these simulations did not achieve a fully turbulent flow within the simulation time and should have been run longer. The

lowest La_t cases yielded 'S' shaped $\overline{w'b'}$ profiles that became positive where they should have become zero. The base of the $\overline{w'b'}$ profile extended all the way to the bottom of the domain in the largest La_t case. Thus, results from the limits of the La_t range may not be trustworthy. From observations, however, La_t typically falls within the range 0.2 – 0.5; the data from simulations corresponding to this shorter range are likely acceptable to analyze for the purposes of a rough approximation.

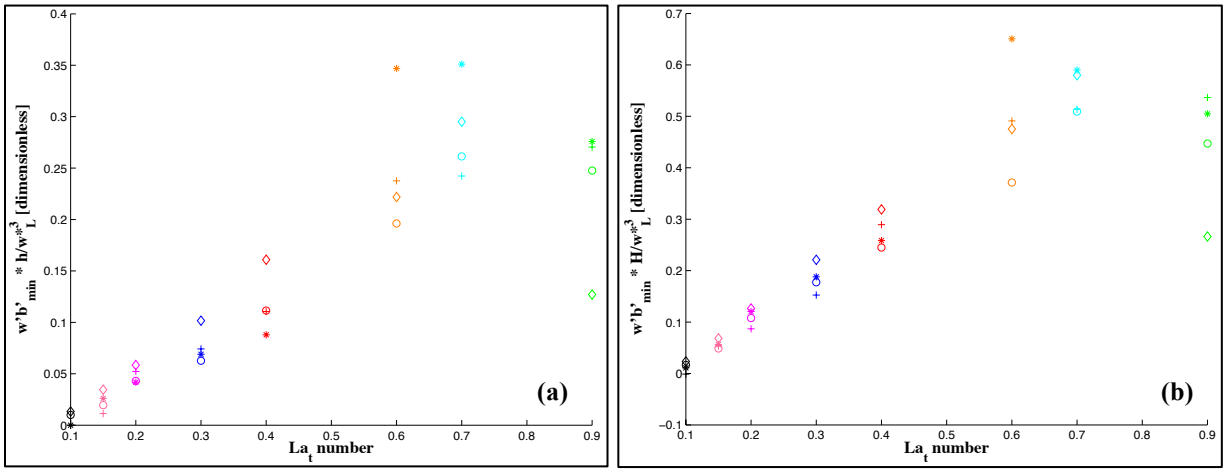

Figure 9. These plots are equivalent to the result of dividing the y-axis by the x-axis in figures 7a and 7b, then organizing data points by turbulent Langmuir number. The colors correspond to La_t and the shapes indicate different combination of wind speed and wave age.

Figure 9 presents the results of the additional simulations with varied La_t. Following results from Grant and Belcher (2009), figure 9a was expected to collapse into a horizontal line centered around 0.095, the slope of the fitted line in figure 7a. This would indicate that the ratio of $\overline{w'b'}_{min}$ to $\frac{w_L^{*3}}{h}$ is independent of La_t. Instead, figure 9a shows that this ratio increases consistently with increasing La_t. Within the region of interest, the 0.2 – 0.5 range of La_t, the relationship between the ratio and La_t is fairly linear, with some vertical spread at each individual La_t representing the previously discussed effect of different wind speeds. Figure 9b plots the same ratio against La_t, but uses the base of the buoyancy production curve as the mixed layer depth. A similar linear trend results, but with slightly less vertical spread than in figure 9a.

This agrees with the previous finding (displayed in figure 7) that treating the base of $\overline{w'b'}$, rather than the depth of minimum $\overline{w'b'}$, as the mixed layer depth yields a tighter linear fit between $\overline{w'b'}_{min}$ and $\frac{w_L^{*3}}{h}$.

Discussion

The simulation conditions for this study differed immensely from those of Grant and Belcher (2009), who used a nonzero Coriolis parameter, higher vertical grid resolution, and surface friction velocities up to an order of magnitude lower than those in this study. From this perspective, it is difficult to judge whether the disparity between this study's results and Grant and Belcher's is indicative of genuine changes in turbulent scaling over large ranges of forcing parameters, or whether this was a consequence of simulation design variation. However, the fact that the lower range data points from this study appear to agree with the 0.045 slope specified by Grant and Belcher (2009) suggests that the two studies are, in fact, comparable and supports the possibility that the minimum buoyancy flux and the depth at which it occurs scale differently at higher winds.

The linear fits plotted in figure 8 provide information about how the rates of production of potential energy and TKE are related to each other. According to Grant and Belcher (2009), the term $\frac{w_L^{*3}}{h}$ represents the rate of production of TKE over the whole mixed layer. The term $\overline{w'b'}_{min}$ denotes the maximum rate of production of potential energy, which occurs through entrainment at the base of the mixed layer. Since the buoyancy flux between the surface and the base of the mixed layer is approximately linear (see figure 5) and zero at the surface, the average value of the buoyancy flux over the mixed layer is $\frac{1}{2}\overline{w'b'}_{min}$. Thus, the linear fit found by Grant and Belcher (2009) and plotted in figure 8 indicates that potential energy is generated within the

mixed layer at approximately 2% of the rate of TKE generation. In contrast, the fit determined by this study implies that this ratio is closer to 5%. However, these calculated ratios are not necessarily helpful quantities, considering the non-linearity apparent in figure 7a. Instead, figure 7a suggests that the rate of production of potential energy increases relative to the rate of production of TKE with higher wind speeds. Furthermore, figure 9a indicates that these ratios of energy production depend additionally on turbulent Langmuir number, whereas Grant and Belcher (2009) found that the ratios are independent of La_t in their low-wind simulations. These results suggest that the scaling theorized by Grant and Belcher (2009) does not fully capture the effects of turbulence on energy production at the surface of the ocean.

It is unclear exactly why this scaling fails to describe turbulent energy production in this study, yet works so cleanly in Grant and Belcher (2009); several possibilities, both individually and in conjunction with each other, may explain the disagreement. First, it is possible that the two LES models, which would ideally yield the same results that are representative of reality, actually produce different results. To test this hypothesis, the simulations specified within this study should be applied to the LES model utilized by Grant and Belcher (2009), or vice versa. A similar problem may originate from issues with grid resolution. The 2-meter vertical resolution used in this study (for comparison, Grant and Belcher (2009) used 0.8m vertical resolution) may be too coarse to capture finer details, such as the exponential decay of Stokes drift velocity and its impact on the Stokes current shear (and rate of generation of TKE across the first layer of grid cells). This study did not test for any dependencies on grid resolution or domain size, but such sensitivity tests would be helpful to identify or dismiss grid domain design as an influence over results. Other crucial model design elements, such as the value of the Coriolis parameter, may have contributed to differences between results. Another possibility is that the scaling simply

does not work well for higher wind stresses, since Grant and Belcher (2009) forced simulations with only low values of u^*. Perhaps there is a hidden dependency on La_t that becomes visible with greater wind and correspondingly larger turbulent energy budgets. Either of these explanations, if true, would indicate that Grant and Belcher's proposed scaling is missing a crucial component and needs to be reexamined.

Initial exploration of the length scale defined by the depth of the buoyancy flux curve's base (H) offers some interesting results. Inputting this length scale in Grant and Belcher's scaling term $\frac{w_L^{*3}}{h}$ in place of h produced a tighter linear fit across all wind speeds than the fit obtained using their originally defined mixed layer depth. Since H is an empirically defined quantity, the linear relationship between $\overline{w'b'}_{min}$ and $\frac{w_L^{*3}}{H}$ does not have the theoretical significance with respect to turbulent energy budgets that Grant and Belcher (2009) attribute to $\frac{w_L^{*3}}{h}$. Nevertheless, the highly linear relationship suggests that H is a useful, potentially significant length scale. Conceptually, H captures a different aspect of the shape of the buoyancy flux curve than h, since it describes the depth to which turbulence extends. Although Grant and Belcher disregard this depth, H is intuitively important: one can imagine that the same depth-integrated amount of rate of potential energy generation, distributed differently through the water column, would result in interestingly different patterns of mixing. Characterizing those differences is beyond the scope of this study, but presents a compelling question for future work.

Conclusions

This study aimed to reproduce the scaling proposed by Grant and Belcher (2009) for a range of higher winds and found that the relationship between $\overline{w'b'}_{min}$ and $\frac{w_L^{*3}}{H}$ becomes slightly nonlinear over larger ranges of u^*. Furthermore, a basic, preliminary analysis of additional

simulation cases indicate that the relationship between these terms depends on the turbulent Langmuir number, disagreeing with Grant and Belcher's findings. These results suggest that the proposed scaling may need reviewing; however, it is necessary to perform sensitivity tests to verify that grid resolution, data output frequency, and averaging windows did not affect the turbulent statistics. Additionally, it is recommended that additional LES simulations are performed with a nonzero Coriolis parameter and low winds, to ensure that model differences did not influence results.

This study also introduced a new definition of mixed layer depth, H, defined by the base of the buoyancy flux curve. Although this depth was calculated only to first-order approximation, it yielded a much tighter linear fit when substituted for mixed layer depth in the Grant and Belcher scaling terms. This length scale may prove effective for purposes of parameterization, since linearity implies predictability and H yielded a linear fit over a large range of realistic u^*. Future work should focus on additional exploration of this depth. The variables that control this depth are currently unknown, and this study did not attempt to identify them. Hypothetically, H could depend on w_L^*, N^2 (buoyancy frequency, a measure of stratification), h, etc. Investigating these dependencies could help improve parameterization of turbulence, but it may also lead to a deeper understanding of the mechanisms controlling entrainment at the base of the mixed layer.

Finally, the simulation design implemented for this study was overly simplistic. Future simulations should investigate if and how these scalings change under the influence of complexities such as time-varied winds, the combined effects of wind and surface cooling, time-varied La_t, a nonzero Coriolis parameter, a wave spectrum (rather than monochromatic waves), and the misalignment of Stokes drift and wind.

Acknowledgements

I would like to thank Baylor Fox-Kemper for being my thesis advisor and contributing the majority of my knowledge of oceans and turbulence. His un*wave*ring enthusiasm for the motions of the oceans and research was a constant source of encouragement and inspiration, especially during the inevitable times when progress trickled to a halt. I am grateful to Baylor for tirelessly answering all my questions – even those posed numerous times throughout the year. I would like to thank Brodie Pearson and Nobuhiro Suzuki for helping me work through tricky bugs in the LES code that I may never have resolved on my own. I am particularly indebted to Brodie, who also provided me with vital guidance regarding data analysis, directed me to several reference papers, and advised me about how to interpret results. I am grateful to Mara Freilich and Katrina Machado for their moral support, and I am incredibly thankful for being so warmly welcomed into the DEEPS community this past year. Finally, I would like to thank Robert Pelcovits for acting as my advisor from the Physics Department, as well as my concentration advisor for the past three years.

References

A. Webb and B. Fox-Kemper (2011). Wave spectral moments and Stokes drift estimation. *Ocean Modelling*, *40* (3-4): 273-288.

A. Webb and B. Fox-Kemper (January 2015). Impacts of wave spreading and multidirectional waves on estimating Stokes drift. *Ocean Modelling*. In press.

Belcher, S.E., A. A. L. M. Grant, K. E. Hanley, B. Fox-Kemper, L. Van Roekel, P. P. Sullivan, W. G. Large, A. Brown, A. Hines, D. Calvert, A. Rutgersson, H. Petterson, J. Bidlot, P. A. E. M. Janssen, and J. A. Polton (2012). A global perspective on Langmuir turbulence in the ocean surface boundary layer. *Geophysical Research Letters*, *39* (18):L18605, 9pp.

Cronin, M.F. and J. Sprintall (2000). Upper Ocean Structure: Wind and Buoyancy-forced Upper Ocean. For publication in the *Encyclopedia of Ocean Sciences*, 1-18.

D'Asaro, E.A., J. Thomson, A. Y. Shcherbina, R. R. Harcourt, M. F. Cronin, M. A. Hemer, and B. Fox-Kemper (2014). Quantifying upper ocean turbulence driven by surface waves. *Geophysical Research Letters*, *41* (1): 102-107.

Garrett, C. (2004) Lecture 8: Tidal Rectification and Stokes Drift [pdf]. Retrieved from Woods Hole Oceanographic Institute Tides course website: http://www.whoi.edu/

Garwood, R.W. (1976). A General Model of the Ocean Mixed Layer. *Pacific Marine Environmental Lab*: Washington. NOAA ERL 384-PMEL 27.

Grant, A. L. M. and S.E. Belcher (2009). Characteristics of Langmuir Turbulence in the Ocean Mixed Layer. *American Meteorological Society, 39*, 1871-1887.

Haney, S., (2015). *Mixing and Restratification in the Upper Ocean: Competing Mechanisms in the Wave-Averaged Boussinesq Equations* (Doctoral Dissertation) Univ of Colorado, Boulder

Harcourt, R.R. and E.A. D'Asaro (2008). Large-Eddy Simulation of Langmuir Turbulence in Pure Wind Seas. *Journal of Physical Oceanography, 38*, 1542-1562.

Li, Q., A. Webb, B. Fox-Kemper, A. Craig, G. Danabasoglu, W. G. Large, and M. Vertenstein. Langmuir mixing effects on global climate: WAVEWATCH III in CESM. *Ocean Modelling*, 2015. Submitted.

McWilliams, J.C., P.P. Sullivan, and C.H. Moeng (1997). Langmuir turbulence in the ocean. *Journal of Fluid Mechanics, 334*, 1-30.

Moeng, C.-H. (1984). A large-eddy-simulation model for the study of planetary boundary layer turbulence. *Journal of the Atmospheric Sciences*, *41* (13), 2052-2062.

Reynolds, O. (1895). On the dynamical theory of incompressible viscous fluids and the determination of the criterion. *Phi/os. Trans*. 186: 123-64.

Sarmiento, J.L. and N. Gruber (2013). *Ocean Biogeochemical Dynamics*. Princeton, NJ: Princeton University Press.

Tejada-Martinez, A.E. et al. (2011). Large-eddy simulation of shallow water Langmuir turbulence using isogeometric analysis and the residual-based variational multiscale method. *Journal of Applied Mechanics*, *79* (1), 1-12.

Thorpe, S.A. (2004). Langmuir Circulation. *Annual Review of Fluid Mechanics*, *36*, 55–79.

Van Roekel, L.P. et al. (2012). The form and orientation of Langmuir cells for misaligned winds and waves. *Journal of Geophysical Research, 117*.

Bouws, E. (1998) *Guide to Wave Analysis and Forecasting*. Secretariat of the World Meteorological Organization.

Appendix

Table 1: Simulation parameters for La_t = 0.3. Note that D_s and u^* have units [m] and [m/s], respectively.

C_p/U_{10}	U_s/U_{10}	U_{10} (m/s):	8.3	11.4	14.8	18.1	21.3	25.8	28.8	32.6
0.6	1.24%	D_s:	0.330	0.622	1.049	1.569	2.173	3.188	3.972	5.090
		u^*:	0.009	0.012	0.016	0.020	0.024	0.029	0.032	0.036
0.8	1.42%	D_s:	0.575	1.085	1.829	2.736	3.789	5.559	6.926	8.875
		u^*:	0.011	0.015	0.019	0.023	0.027	0.033	0.037	0.042
1	1.53%	D_s:	0.839	1.583	2.668	3.991	5.527	8.108	10.104	12.946
		u^*:	0.011	0.016	0.020	0.025	0.029	0.036	0.040	0.045
1.2	1.75%	D_s:	1.249	2.356	3.971	5.939	8.225	12.067	15.036	19.266
		u^*:	0.013	0.018	0.023	0.029	0.034	0.041	0.045	0.051

Table 2: Simulation parameters for varied La_t. Note that u^* has units [m/s].

C_p/U_{10}	U_s/U_{10}	D_s[m], U_{10}[m/s]	La_t:	0.1	0.15	0.2	0.4	0.6	0.7	0.9
0.6	1.24%	D_s: 1.049 U_{10}: 14.8	u^*:	0.0018	0.0041	0.0073	0.0294	0.0661	0.0899	0.1487
		D_s: 3.972 U_{10}: 28.8	u^*:	0.0036	0.0080	0.0143	0.0571	0.1286	0.1750	0.2893
1.2	1.75%	D_s: 3.971 U_{10}: 14.8	u^*:	0.0026	0.0058	0.0104	0.0414	0.0932	0.1269	0.2098
		D_s: 15.04 U_{10}: 28.8	u^*:	0.0050	0.0113	0.0202	0.0806	0.1814	0.2470	0.4082